



A microfluidic flow-focusing device for low sample consumption serial synchrotron crystallography experiments in liquid flow

Diana C. F. Monteiro,^a Mohammad Vakili,^{a,‡} Jessica Harich,^{a,‡} Michael Sztucki,^b Susanne M. Meier,^a Sam Horrell,^a Inokentijis Josts^{a,c} and Martin Trebbin^{d,a,*}

Received 8 October 2018

Accepted 7 January 2019

Edited by R. W. Strange, University of Essex, UK

‡ These authors contributed equally to this work.

Keywords: serial synchrotron crystallography; microfluidics; flow focusing.

Supporting information: this article has supporting information at journals.iucr.org/s

^aThe Hamburg Centre for Ultrafast Imaging, Universität Hamburg, Luruper Chaussee 149, Hamburg 22761, Germany, ^bESRF, European Synchrotron Radiation Facility, 71 Avenue des Martyrs, Grenoble CS 40220, France, ^cDepartment of Chemistry, Universität Hamburg, Martin-Luther-King-Platz 6, Hamburg 20146, Germany, and ^dDepartment of Chemistry, University at Buffalo, State University of New York, 359 Natural Sciences Complex, Buffalo, NY 14260-3000, USA. *Correspondence e-mail: mtrebbin@buffalo.edu

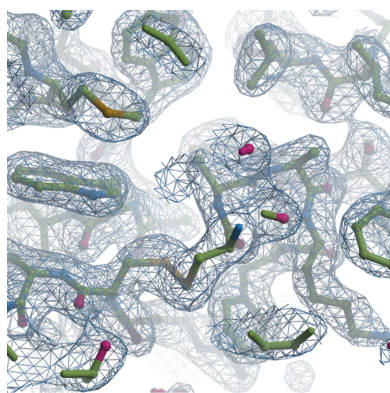
Serial synchrotron crystallography allows low X-ray dose, room-temperature crystal structures of proteins to be determined from a population of microcrystals. Protein production and crystallization is a non-trivial procedure and it is essential to have X-ray-compatible sample environments that keep sample consumption low and the crystals in their native environment. This article presents a fast and optimized manufacturing route to metal–polyimide microfluidic flow-focusing devices which allow for the collection of X-ray diffraction data in flow. The flow-focusing conditions allow for sample consumption to be significantly decreased, while also opening up the possibility of more complex experiments such as rapid mixing for time-resolved serial crystallography. This high-repetition-rate experiment allows for full datasets to be obtained quickly (~1 h) from crystal slurries in liquid flow. The X-ray compatible microfluidic chips are easily manufacturable, reliable and durable and require sample-flow rates on the order of only 30 $\mu\text{l h}^{-1}$.

1. Introduction

Microfluidic devices have emerged as platforms for X-ray scattering and diffraction experiments at both synchrotrons and XFELs (X-ray free-electron lasers) (Ghazal *et al.*, 2016; Narayanan *et al.*, 2017; Sui & Perry, 2017; Trebbin *et al.*, 2013). These sample environments allow for the accurate handling of microlitre fluid flows in micrometre-sized channels. The sample can be continuously flowed inside the microfluidic chip. X-ray-induced damage to the sample during data collection is greatly reduced due to the constant replenishment at the X-ray interaction region (Köster & Pfohl, 2012; Jeffries *et al.*, 2015; Pernot *et al.*, 2010). When employing microcrystalline slurries as samples, single diffraction patterns from individual flowing microcrystals can be collected in a serial synchrotron crystallography (SSX) approach, as described below.

Several metal–polyimide (metal–Kapton) X-ray compatible microfluidic devices have been previously described for *in situ* X-ray scattering experiments. The devices have been used to follow global structural transitions of proteins upon diffusion of ligands or under re-folding conditions (Dootz *et al.*, 2006; Ghazal *et al.*, 2016; Graceffa *et al.*, 2013) and structural transitions in polymers (Iida *et al.*, 2009; With *et al.*, 2014).

So far, the most widely used techniques to seal polyimide–metal devices required either clamping of the foils with external plates (Uzawa *et al.*, 2004; Graceffa *et al.*, 2013), the



use of silicone-based self-adhesive polyimide (Dootz *et al.*, 2006; Köster *et al.*, 2008; Pfohl *et al.*, 2007) or the use of epoxy glue (Iida *et al.*, 2009). There are two further methods for the bonding of polyimide foils to produce microfluidic devices, though these are not as widely used. The first involves surface modification chemistry (Heymann *et al.*, 2014). While this approach can yield Kapton-based devices with a very low X-ray background, the process adds manual fabrication steps that can lower the reproducibility of bonding quality. The reagents also degrade over time, further impacting the manufacturing procedure. A second approach employs heat sealing of polyimide foils coated with a thin layer of a melt-processable fluoro-polymer. This method has been shown to allow the fabrication of chemically inert and pressure-resistant microfluidic devices for X-ray experiments (With *et al.*, 2014; Barrett *et al.*, 2006). This approach also offers a very reproducible, single-step bonding routine.

Even though these heat-sealed Kapton-based devices are highly X-ray resistant, they have yet to be used in flow-based SSX experiments. SSX differs from standard macromolecular crystallography in that thousands of static diffraction patterns are collected from individual microcrystals, in contrast to the collection of rotation series of one or a few single large crystals, allowing for room-temperature diffraction data to be collected without severe X-ray radiation damage (Warkentin *et al.*, 2012). Compared with cryo-cooling-based measurements that could introduce structural artefacts, room-temperature measurements avoid these and reveal the conformational flexibility of proteins (Fraser *et al.*, 2011).

SSX has required the development of new sample delivery methods (Yamamoto *et al.*, 2017); these include, for example, fixed targets (Owen *et al.*, 2017), an X-ray-compatible conveyor belt with either drop-on demand (Roessler *et al.*, 2013) or liquid dispensers (Beyerlein *et al.*, 2017), or high-viscosity extruders (Botha *et al.*, 2015; Nogly *et al.*, 2015). In fixed targets, the microcrystalline slurry is spread onto an X-ray-compatible chip [made of silicon (Roedig *et al.*, 2016; Zarrine-Afsar *et al.*, 2012; Mueller *et al.*, 2015), silicon nitride (Coquelle *et al.*, 2015) or polymers (Huang *et al.*, 2015; Baxter *et al.*, 2016; Axford *et al.*, 2016; Schubert *et al.*, 2016)], and diffraction patterns are collected while the chip is rastered through the X-ray beam (Owen *et al.*, 2017). For high-viscosity extruders, the crystals are embedded in a highly viscous medium, such as a lipidic cubic phase (Weinert *et al.*, 2017), grease or hydrogels (Kováčsová *et al.*, 2017; Sugahara *et al.*, 2015). All these approaches have been shown to produce good quality SSX data. Nevertheless, they require the handling and transfer of the microcrystalline slurry, which may be detrimental for samples that are sensitive to changes in environment. They are also not amenable for *in situ* fast delivery of ligands on the millisecond timescale and, therefore, cannot be used for rapid-mixing experiments. On the other hand, microfluidics pave the way for millisecond-mixing-based time-resolved structural experiments at modern synchrotron and FEL sources, where systems are perturbed from equilibrium and their subsequent structural changes tracked in real time (Svergun *et al.*, 2013). Recent examples include the mixing of

small-molecule actuators to observe functional structural intermediates of proteins and nucleic acids (Stagno *et al.*, 2017; Denz *et al.*, 2017; Olmos *et al.*, 2018) as well as the study of phase transitions of polymeric nanoparticles (Karnik *et al.*, 2008; Wang *et al.*, 2011; Fürst *et al.*, 2016).

In-flow SSX was first reported by Stellato *et al.* who showed that diffraction can be collected from microcrystals in flow in a 100 μm glass capillary (Stellato *et al.*, 2014). Their approach involves flowing a microcrystalline slurry through the capillary and using short X-ray exposures with a microbeam to capture single diffraction patterns from single crystals (Stellato *et al.*, 2014; Standfuss & Spence, 2017). Even though this approach was first demonstrated in 2014, no further optimizations, such as the introduction of microfluidic chips, have yet been reported for SSX. Since protein production and crystallization are challenging, especially in large quantities, flow-focusing approaches, where the sample is centered in a fluid stream by co-flowing with a coaxial aqueous medium, can diminish sample consumption by markedly reducing the width of the sample flow. Flow-focusing has already been shown to maintain the high concentration of the macromolecular sample in the central region of the device in SAXS experiments (Denz *et al.*, 2017). Here, we show that this approach can also be used for diffraction experiments, that the sample remains centered on the chip and can be aligned to the X-ray interaction region, and that the indexable hit-rate is indeed comparable with that quoted by Stellato *et al.* (2014) for a non-flow-focused sample.

2. Results and discussion

2.1. Device manufacture

Kapton FN is a polyimide foil which is coated on one side with a melt-processable 25 μm thin layer of FEP (fluorinated ethylene propylene copolymer). FEP, a highly inert polymer, was used to create a strong and durable metal–polyimide microfluidic device suitable for X-ray scattering and diffraction experiments. The polymer properties of FEP, specifically its melting temperature in combination with a quick surface-plasma activation step, allowed for a very repeatable and reliable manufacturing workflow whereby tightly sealed, leak-free and reproducible devices could be easily made and did not require any external bulky clamps. The devices presented here are novel in the sense that they are a hybrid of previously reported methodologies. Heat-sealable Kapton foils have been previously employed to fabricate thin, pure Kapton devices where the microfluidic channels were produced by laser-ablation techniques (With *et al.*, 2014; Barrett *et al.*, 2006). Kapton–metal hybrid devices, where the channels are produced through spark erosion of metal plates, have been reported bearing either self-adhesive polyimide foils (weak bonding, silicon-based coating) or bound through surface chemistry. We built on these two previously described methods and developed a fast and optimized fabrication routine for the bonding of Kapton FN foils to metal microfluidic chips under controlled temperature and pressure using a hot press (for the detailed procedure, see the *Experimental*

section). Spark erosion of metal plates allows for a CAD-structure-based parallel, large-scale production of microfluidic chips, compared with the highly time-consuming laser ablation method used for structuring Kapton foils. Our method utilizes lower temperatures than previously described (270°C versus the previously reported $300\text{--}370^{\circ}\text{C}$), does not require controlled-temperature ramping and is completed within 20 min. This temperature is slightly above the FEP melting temperature, allowing it to bond to the metal chip without flowing into the microchannels. The procedure was optimized to yield bubble-free and strongly bound devices. The chemical resistance of the FEP, heat sealability and thinness made the device ideal for X-ray diffraction experiments.

An overview of the device geometry and fabrication is shown in Fig. 1. A cross-shaped junction at the top of the chip brings together three fluid inlets, the central one for the sample and two side channels for buffers, which flow along the main channel where the crystals are probed by X-rays (Fig. 2). The square channels ($300\ \mu\text{m} \times 300\ \mu\text{m}$) were spark eroded into a metal plate.

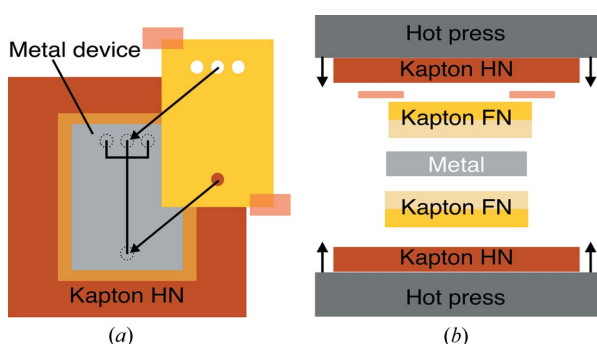


Figure 1 Schematic representation of the hot-press-assisted fabrication procedure for the microfluidic device. (a) Overview of the device layers and alignment. (b) Layer stacking inside the hot press for bonding. The metal frame is sandwiched between two Kapton FN foils. The hot plates are protected with two Kapton HN foils to avoid attachment of the device to the hot press. The plates are heated and sealed during bonding.

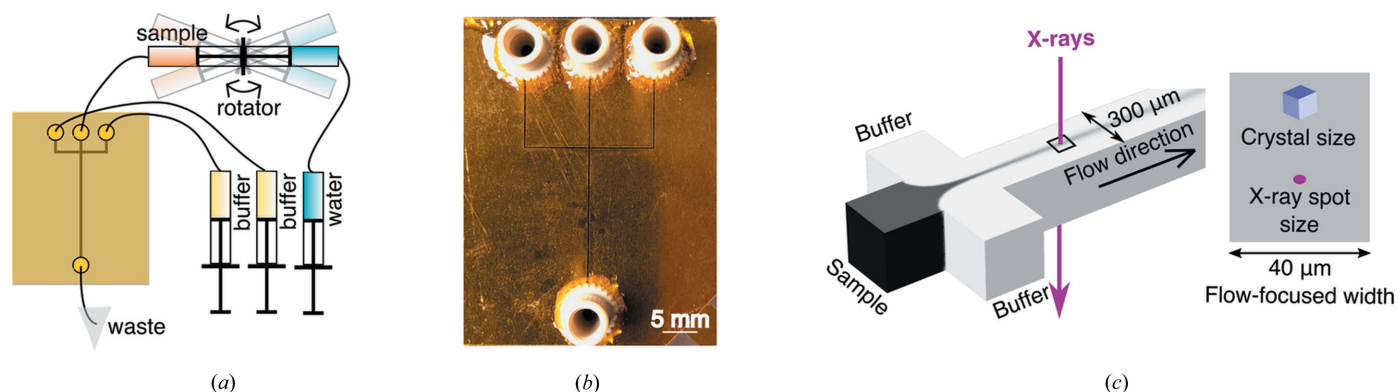


Figure 2 Overview of the experimental setup. (a) Device and fluidic connections. The sample flows in the center channel and the buffer flows in the side channels. The microcrystalline slurry sample is placed in a sample reservoir on an anti-settling device. The sample flow is controlled by injection of water into the reservoir which hydraulically flows the sample into the device. (b) The polyimide metal device showing the attached nanoports for fluid connections. (c) Schematic view of a 10:1 flow-focusing of the sample by the buffer (total flow rate $330\ \mu\text{l h}^{-1}$). The cross-sectional area of the device channel is $300\ \mu\text{m} \times 300\ \mu\text{m}$ and the width of the flow-focused stream is roughly $40\ \mu\text{m}$. The crystal size and X-ray spot size are shown to scale. The sample is irradiated through the volume of water encapsulated by polyimide windows.

2.2. Experimental design and data collection

X-ray-transparent metal–polyimide devices make use of cut-through channels in thin steel metal plates which are then sealed with polyimide foils. Here, a $300\ \mu\text{m} \times 300\ \mu\text{m}$ channel size was chosen to accommodate the minimum workable sample flow rate of $30\ \mu\text{l h}^{-1}$ in order to prevent settling in the sample feeding lines and device entrance which quickly leads to clogging. The cross-shaped junction allows for the sample to be flow-focused hydrodynamically with buffer which confines the sample in a region where the fluid streamlines are more uniform, allowing for controlled diffusion. At high buffer-to-sample flow ratios, the crystal flow is centered in the channel, maintaining a very stable and constant speed of microcrystals as well as a good overlap with the X-ray microbeam. Flow-focusing therefore decreases sample consumption while maintaining the sample-residency time in the X-ray beam as needed. As the sample is flow-focused, there is largely no sample-dilution effect and thus no decrease of hit-rate. Crystal diffusion out of the liquid stream is negligible due to the very small diffusion coefficients of these micrometre-sized species ($\sim 1 \times 10^{-13}\ \text{m}^2\ \text{s}^{-1}$ for a $5\ \mu\text{m}$ crystal and $\sim 4 \times 10^{-14}\ \text{m}^2\ \text{s}^{-1}$ for a $10\ \mu\text{m}$ crystal).

A 10:1 flow-focusing regime ($2 \times 150\ \mu\text{l h}^{-1}$ buffer and $30\ \mu\text{l h}^{-1}$ sample) provided sufficient crystal residency time in the X-ray beam for diffraction to be collected. The sample speed in the center of the device was calculated to be $1.9\ \text{mm s}^{-1}$, giving a maximum residency time of 5 ms for the fastest flowing $10\ \mu\text{m}$ crystals and an X-ray beam size of $2.7\ \mu\text{m} \times 3.7\ \mu\text{m}$. The $300\ \mu\text{m}$ thickness of the chip along with the thin polyimide windows ($2\ \mu\text{m} \times 25\ \mu\text{m}$ Kapton) also delivered a relatively low background.

Data were collected at beamline ID13 at the European Synchrotron Radiation Facility (ESRF). Lysozyme crystals ($8\text{--}12\ \mu\text{m}$) were used as the test sample. The crystalline slurry was placed in a sample reservoir mounted on a slowly alternating rotation motor which acted as an anti-settling device (Fig. 2). The liquid-flow rates were controlled using high-precision

syringe pumps and the device and crystal flow were aligned to the X-ray interaction region. The combination of a very bright microbeam [$3.7 \mu\text{m} \times 2.7 \mu\text{m}$ (H \times V) FWHM, 2×10^{12} photons s^{-1}] with the recording of diffraction patterns on an Eiger X 4M detector (Dectris AG) allowed for diffraction patterns to be collected from very short exposures (1.4 ms) at very high repetition rates (715 Hz).

One of the main problems with the use of microfluidic devices and aqueous solutions is the rapid formation of X-ray radiation-induced H_2 bubbles as well as the fouling of the device windows with degraded sample, both of which can rapidly disrupt the fluid flow. Fouling of the windows is especially problematic for SAXS and WAXS experiments as it causes a change in background that cannot be easily modeled. For diffraction, small changes to the background are more easily modeled as the background is calculated locally, *i.e.* the area on the detector adjacent to the diffraction peak for every Bragg-spot. The main disruption due to fouling in SSX is in fact when the flow is disrupted by the accumulated material. This effect, as well as the appearance of bubbles, manifests as a drop in live diffraction hit-rate which was monitored in real time using *NanoPeakCell* (Coquelle *et al.*, 2015). As a consequence, the data collection strategy was altered and optimized accordingly to prevent both the accumulation of debris and the formation of bubbles (Fig. 3). In our optimized data collection strategy (see Section 3.3), we worked in 2 s increments, each composed of 0.28 s of X-ray exposure (a burst of 200 detector images) and a waiting time of 1.72 s, during which the sample is still flowing. This waiting time was dictated by the necessary detector image transfer speed and can most likely be decreased in future by using faster connections resulting in a lower sample consumption for the overall dataset. However, a minimum waiting time will always be needed to allow for dissipation of any hydrogen/hydroxyl radicals to occur and is expected to be short due to the very high diffusion coefficient of these species [OH^\bullet $7.1 \mu\text{m}^2 \text{s}^{-1}$ (Campo & Grigera, 2005)]. Each dataset was 40 000 images, took ~ 6.67 min in total to be collected (200×2 s increments with 200 images each, including waiting time) and was followed by 2 min of sample

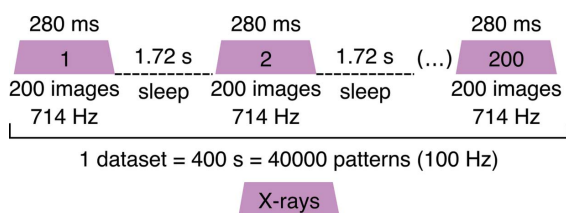


Figure 3

The data collection strategy, showing the X-ray shutter opening and closing cycle. 200 images of 1.4 ms each are collected in each X-ray burst, with 1.72 s of no X-rays in between. The cycle is repeated 200 times for each dataset.

Table 1

Data collection, reduction and structure solution statistics.

Data collection parameters		Refinement parameters	
PDB code	6h79	Total reflections	7428 (536)
Temperature (K)	293	No. reflections R_{free}	400 (21)
Exposure/image (ms)	1.4	R_{work}	0.166 (0.318)
X-ray dose (kGy)†	100	R_{free}	0.216 (0.356)
Total images	320 000	No. atoms	1059
Total measurement time	~ 1 h 10 min	Protein	1017
No. indexable hits (hit rate)	5349 (1.7%)	Ligand/ion	10
Space group	$P4_32_12$	Water	32
Unit-cell parameters		B factors (\AA^2)	
$a = b$ (\AA)	79.3	Protein	53.68
c (\AA)	37.7	Ligand/ion	61.99
$\alpha = \beta = \gamma$ ($^\circ$)	90	Water	53.70
Resolution (\AA)	56.07–2.10 (2.16–2.10)	Ramachandran plot (%)	
$\langle\langle I/\sigma(I) \rangle\rangle$	5.57 (1.36)	Favored	96.06
Completeness (%)	100 (100)	Allowed	3.94
Multiplicity	121.1 (87.6)	Outliers	0.00
R_{split} (%)	11.6 (113)	R.m.s. deviations	
$\text{CC}_{1/2}$	0.96 (0.32)	Bond lengths (\AA)	0.009
CC^*	0.99 (0.70)	Bond angles ($^\circ$)	1.548
Wilson B factor (\AA^2)	43.9	Clashscore	5

† Diffraction-weighted dose calculated using *Raddose3D* (Zeldin, Gerstel *et al.*, 2013).

flushing for good sample refreshment. Eight datasets were collected (320 000 images in total) giving a total acquisition time of 4160 s (77 Hz effective average, 1 h 10 min total). From these patterns, more than 5300 could be indexed (1.7% indexable hit-rate) and a lysozyme structure to a resolution of 2.1 \AA was determined (Fig. 4). The diffraction-weighted dose for the experiment was 100 kGy, which is well below the dose limit for room-temperature data collection from a single lysozyme crystal (Barker *et al.*, 2009; Garman, 2010; Zeldin, Brockhauser *et al.*, 2013).

The data collection parameters, data reduction statistics and model building statistics are reported in Table 1 and show that the data quality is comparable with that reported for previous SSX data collected in flow (Stellato *et al.*, 2014). The indexable hit rate obtained is also comparable with that reported by Stellato *et al.*, where data were collected in flow using a simple 100 μm glass capillary as the sample environment. It is

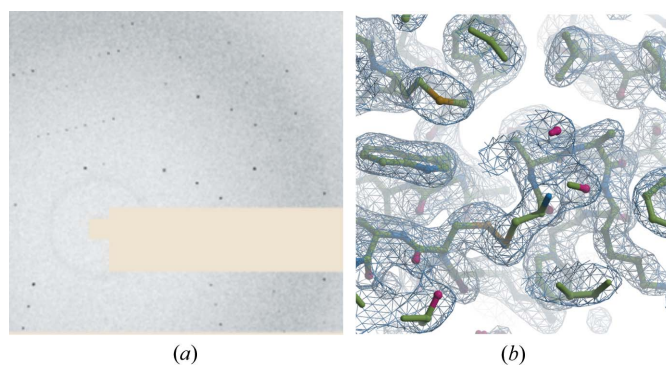


Figure 4

Example of X-ray data. (a) Section of a diffraction pattern collected showing clean diffraction spots. (b) Part of the lysozyme protein chain. Carbon atoms are shown in green, oxygen in red, nitrogen in blue and sulfur in yellow. A $2F_o - F_c$ electron-density map contoured at 1 r.m.s.d. is shown as a blue mesh.

important to note that the sample consumption of our experiment during data collection is five times lower. The indexable hit rate achieved here was noteworthy as the exposure times for each pattern were very short and the X-ray beam size was very small. In this experiment, the sample volume probed by the X-ray beam for each image (obtained by taking into account the beam size, sample depth and flow speed) was approximately ten times smaller than that reported by Stellato *et al.*, but the crystals used here were approximately five times larger by volume (Fig. S1 of the supporting information). These results show that flow-focusing does not cause large dilution effects and that it works well in keeping the high-density crystal flow in the center of the device. The flow-focusing approach therefore allows for a large decrease in sample consumption compared with single-flow devices, without sacrificing the number of useable frames in the dataset. The short exposure time and high repetition rate of this experiment lead to a considerable decrease in the overall data collection time needed to obtain a full dataset for structure solution compared with previous in-flow SSX experiments (Stellato *et al.*, 2014).

3. Experimental

3.1. Device fabrication

The 300 μm -thick Cr–Ni alloy metal plates (H+S Präzisions-Folien GmbH) were spark eroded to yield 300 μm -wide microchannels with 1.5 mm-wide circular inlets and outlets. This microstructuring was performed using high-voltage wire erosion on an AGIE AC X CLASSIC V3 with a 250 μm brass wire. A DXF file created with *AutoCAD* 2017 (Autodesk) contained the channel geometry which was translated into the trajectory of the wire.

The device was sealed with two Kapton FN sheets: 25 μm polyimide foil coated on one side with a 25 μm layer of FEP. The polyimide foils were cut to match the size of the metal chip. Then 2 mm-wide inlets were cut using a metal puncher on one foil. The foils were washed in isopropanol and dried with compressed air. The metal chips were sonicated in acetone, washed in isopropanol and dried with compressed air. The surfaces were plasma activated and cleaned in air (0.38 mbar) in a 13.56 MHz ATTO plasma cleaner (Diener Electronic) at 50 W for 10 min. The metal chip was sandwiched between the two Kapton FN layers and the inlets were aligned. Fixation was achieved using polyimide adhesive tapes. The sandwich stack was placed between the two additional 125 μm Kapton HN foils and into a 270°C pre-heated manual hot press (Vogt Labormaschinen GmbH). A series of different pressure steps were employed as follows: 1 kN for 20 s, 20 kN for 10 s (to remove air bubbles), pressure released for <1 s, 1 kN for 10 s, pressure released for <1 s and 1 kN for 14 min 20 s. The bound device was removed from the hot press and allowed to cool to room temperature.

NanoPorts (IDEX) were centered on the inlets and outlet and glued with two-component epoxy glue. OD PE tubing,

1.09 mm in length (Scientific Commodities), was connected to the ports using fingertight fittings and nanotight sleeves.

3.2. Sample preparation and flow

Lysozyme microcrystals were obtained following a previously described protocol (Beyerlein *et al.*, 2017): the crystallization was performed at 1°C to yield 10 μm crystals. All solutions were filtered through a 200 nm filter and cooled to 2°C. A volume of 300 μl protein solution [120 mg ml⁻¹ Lysozyme (Sigma–Aldrich) in 50 mM sodium acetate pH 3.5] was mixed rapidly with 900 μl of precipitant (1M NaCl, 35% *v/v* ethylene glycol, 12.5% *w/v* PEG 3350 and 50 mM acetate pH 3.5). After 30 s at 2°C, the temperature was dropped to 1°C and the mixture vortexed every 2–3 min for 10 s for a total of 15 min. The 10 μm crystals formed within 30 min with a yield of $\sim 1 \times 10^7$ microcrystals ml⁻¹. Accurate temperature control was achieved by using a ThermoStat C equipped with a 2 ml SmartBlock (Eppendorf).

Shortly before the diffraction experiment, the crystal concentration was doubled by removing 50% of the mother-liquor volume. The crystals were loaded into a sample reservoir composed of two 1 ml plastic Luer lock syringes connected with one common double-headed plunger [Fig. 2(a)] and placed on an anti-settling device. Double-filtered water in a 1 ml Hamilton glass gas-tight syringe was used to drive the flow of sample from the reservoir. Buffers were loaded into 2.5 ml Hamilton gas-tight glass syringes. The buffer syringes and sample reservoir were connected to the device feeding lines and nMESYS (Cetoni GmbH) low-pressure syringe–pump modules were used to control the liquid flows of the buffer (150 $\mu\text{l h}^{-1}$) and sample (30 $\mu\text{l h}^{-1}$).

3.3. Data collection and reduction

Data were collected on beamline ID13 (ESRF). The device was aligned to the X-ray interaction region. Data were collected 1 mm vertically below the center of the T-junction. The X-ray beam was 3.7 $\mu\text{m} \times 2.7 \mu\text{m}$ (H \times V) FWHM in size, had a flux of 2×10^{12} photons s⁻¹ and an energy of 13 keV. The 1.4 ms exposures were acquired using an Eiger 4M detector (2070 pixels \times 2167 pixels, pixel size 75 $\mu\text{m} \times 75 \mu\text{m}$; Dectris AG) at a distance of 94.5 mm.

The 200 increments of 200 images (1.4 ms per image, 714 Hz repetition rate) were collected for each individual dataset. The shutter was kept open for the 200-image burst (0.28 s) and closed for 1.72 s between bursts (Fig. 3). The total X-ray exposure time for each dataset of 40 000 images (200 increments \times 200 images) was 400 s with a total acquisition time of ~ 6.67 min including waiting time. A total of eight datasets (32 000 images) were collected with 2 min of flushing time between each dataset for good sample refreshment. The total data collection time was ~ 4160 s (1 h 10 min, 77 Hz average repetition rate).

Live hit rates were monitored using *NanoPeakCell* (Coquelle *et al.*, 2015). The diffraction images were integrated and merged using *CrystFEL* (White *et al.*, 2016) by invoking *MOSFLM* (Battye *et al.*, 2011), *DirAx* (Duisenberg, 1992) and

TakeTwo (Ginn *et al.*, 2016) for integration and *Partialator* (White, 2014) for merging. *Rsplit*, *CC**, *CC1/2*, *SNR*, multiplicity and completeness were calculated with *compare_hkl* and *check_hkl* (CrystFEL). Merged data were phased by molecular replacement with PDB entry 5mjj using *Molrep* (Vagin & Teplyakov, 1997) and refined using *REFMAC5* (Murshudov *et al.*, 2011) within *CCP4i2* (Potterton *et al.*, 2018). Manual model building and real-space refinement was performed using *Coot* (Emsley *et al.*, 2010). The diffraction-weighted dose was calculated using *RADDOSE-3D* (Zeldin, Gerstel *et al.*, 2013).

4. Conclusions

This work is the first demonstration of the possibility of collecting SSX data from flow-focused samples in microfluidic devices. The flow-focusing approach allows for low sample consumption ($30 \mu\text{l h}^{-1}$) and full datasets can be collected in just over 1 h without large dilution effects. To the best of our knowledge, this is also the highest repetition rate SSX experiment at a monochromatic source reported to date. Therefore, this easy-to-fabricate microfluidic polyimide–metal device is very suitable for SSX data collection.

Although the sample consumption over time is still larger than that for viscous jets, the total sample needed for a single dataset is of the same order. The microfluidic liquid flow-focusing approach also opens up the possibility for time-resolved experiments using rapid mixing, through diffusion of small molecules between the sample and buffer flows. The time resolution is defined by the diffusion time of the ligand into the flow-focused sample. The estimated time for a small molecule to diffuse to the center of the flow-focused stream ($20 \mu\text{m}$) is on the order of $\sim 20\text{--}30$ ms (Makinen & Fink, 1977; Schmidt, 2013), which is longer than the current 1.4 ms exposure time necessary to obtain useable diffraction patterns. The use of a small X-ray microbeam also allows rastering across the channel and targeting of species that may form at the fluid interfaces and at different time points along the continuous flow. One further advantage of these devices is the ease of sample handling. The crystals are flowed in their mother liquor (or any other aqueous solution desired) inside a fully sealed device. Minimal handling of the crystals means that samples that are sensitive to changes in humidity or mechanical stress can be studied without damaging them. The microfluidic device presented here was also successfully tested in-house for compatibility with other typical crystallization solutions (such as $2M$ ammonium sulfate, data not shown), indicating that the devices are compatible with a variety of aqueous solutions, as expected given the highly inert nature of both FEP and Kapton, although care must be taken to avoid metal-reactive solutions. The devices can operate without interruption for multiple hours.

Acknowledgements

We thank Arwen Pearson for several useful discussions. We are grateful to Tilman Grunewald and Manfred Burghammer

at the ESRF for providing further assistance during the beam time. We thank Christian Reimer from the mechanical workshop at the University of Hamburg for electric-discharge machining.

Funding information

The experiment was performed on beamline ID13 at the European Synchrotron Radiation Facility (ESRF), Grenoble, France (proposal No. MX-1919). The following funding is also acknowledged: Deutsche Forschungsgemeinschaft (award No. Exzellenzcluster 1074); Bundesministerium für Bildung und Forschung (grant No. 05K16GUI).

References

- Axford, D., Aller, P., Sanchez-Weatherby, J. & Sandy, J. (2016). *Acta Cryst.* **F72**, 313–319.
- Barker, A. I., Southworth-Davies, R. J., Paithankar, K. S., Carmichael, I. & Garman, E. F. (2009). *J. Synchrotron Rad.* **16**, 205–216.
- Barrett, R., Faucon, M., Lopez, J., Cristobal, G., Destremaut, F., Dodge, A., Guillot, P., Laval, P., Masselon, C. & Salmon, J.-B. (2006). *Lab Chip*, **6**, 494–499.
- Battye, T. G. G., Kontogiannis, L., Johnson, O., Powell, H. R. & Leslie, A. G. W. (2011). *Acta Cryst.* **D67**, 271–281.
- Baxter, E. L., Aguila, L., Alonso-Mori, R., Barnes, C. O., Bonagura, C. A., Brehmer, W., Brunger, A. T., Calero, G., Caradoc-Davies, T. T., Chatterjee, R., Degrado, W. F., Fraser, J. S., Ibrahim, M., Kern, J., Kobilka, B. K., Kruse, A. C., Larsson, K. M., Lemke, H. T., Lyubimov, A. Y., Manglik, A., McPhillips, S. E., Norgren, E., Pang, S. S., Soltis, S. M., Song, J., Thomaston, J., Tsai, Y., Weis, W. I., Woldeyes, R. A., Yachandra, V., Yano, J., Zouni, A. & Cohen, A. E. (2016). *Acta Cryst.* **D72**, 2–11.
- Beyerlein, K. R., Dierksmeyer, D., Mariani, V., Kuhn, M., Sarrou, I., Ottaviano, A., Awel, S., Knoska, J., Fuglerud, S., Jönsson, O., Stern, S., Wiedorn, M. O., Yefanov, O., Adriano, L., Bean, R., Burkhardt, A., Fischer, P., Heymann, M., Horke, D. A., Jungnickel, K. E. J., Kovaleva, E., Lorbeer, O., Metz, M., Meyer, J., Morgan, A., Pande, K., Panneerselvam, S., Seuring, C., Tolstikova, A., Lieske, J., Aplin, S., Roessle, M., White, T. A., Chapman, H. N., Meents, A. & Oberthuer, D. (2017). *IUCrJ*, **4**, 769–777.
- Botha, S., Nass, K., Barends, T. R. M., Kabsch, W., Latz, B., Dworkowski, F., Foucar, L., Panepucci, E., Wang, M., Shoeman, R. L., Schlichting, I. & Doak, R. B. (2015). *Acta Cryst.* **D71**, 387–397.
- Campo, M. G. & Grigera, J. R. (2005). *J. Chem. Phys.* **123**, 084507-1–6.
- Coquelle, N., Brewster, A. S., Kapp, U., Shilova, A., Weinhausen, B., Burghammer, M. & Colletier, J.-P. (2015). *Acta Cryst.* **D71**, 1184–1196.
- Denz, M., Brehm, G., Hémonnot, C. Y. J., Spears, H., Wittmeier, A., Cassini, C., Saldanha, O., Perego, E., Diaz, A., Burghammer, M. & Köster, S. (2017). *Lab Chip*, **18**, 171–178.
- Dootz, R., Otten, A., Köster, S., Struth, B. & Pfohl, T. (2006). *J. Phys. Condens. Matter*, **18**, S639–S652.
- Duisenberg, A. J. M. (1992). *J. Appl. Cryst.* **25**, 92–96.
- Emsley, P., Lohkamp, B., Scott, W. G. & Cowtan, K. (2010). *Acta Cryst.* **D66**, 486–501.
- Fraser, J. S., van den Bedem, H., Samelson, A. J., Lang, P. T., Holton, J. M., Echols, N. & Alber, T. (2011). *Proc. Natl Acad. Sci.* **108**, 16247–16252.
- Fürst, C., Zang, P., Roth, S. V., Drechsler, M. & Forster, S. (2016). *Polymer*, **107**, 434–444.
- Garman, E. F. (2010). *Acta Cryst.* **D66**, 339–351.
- Ghazal, A., Lafleur, J. P., Mortensen, K., Kutter, J. P., Arleth, L. & Jensen, G. V. (2016). *Lab Chip*, **16**, 4263–4295.

- Ginn, H. M., Roedig, P., Kuo, A., Evans, G., Sauter, N. K., Ernst, O. P., Meents, A., Mueller-Werkmeister, H., Miller, R. J. D. & Stuart, D. I. (2016). *Acta Cryst. D* **72**, 956–965.
- Graceffa, R., Nobrega, R. P., Barrea, R. A., Kathuria, S. V., Chakravarthy, S., Bilsel, O. & Irving, T. C. (2013). *J. Synchrotron Rad.* **20**, 820–825.
- Heymann, M., Ophthalage, A., Wierman, J. L., Akella, S., Szebenyi, D. M. E., Gruner, S. M. & Fraden, S. (2014). *IUCrJ*, **1**, 349–360.
- Huang, C.-Y., Olieric, V., Ma, P., Panepucci, E., Diederichs, K., Wang, M. & Caffrey, M. (2015). *Acta Cryst. D* **71**, 1238–1256.
- Iida, K., Chastek, T. Q., Beers, K. L., Cavicchi, K. A., Chun, J. & Fasolka, M. J. (2009). *Lab Chip*, **9**, 339–345.
- Jeffries, C. M., Graewert, M. A., Svergun, D. I. & Blanchet, C. E. (2015). *J. Synchrotron Rad.* **22**, 273–279.
- Karnik, R., Gu, F., Basto, P., Cannizzaro, C., Dean, L., Kyei-Manu, W., Langer, R. & Farokhzad, O. C. (2008). *Nano Lett.* **8**, 2906–2912.
- Köster, S., Evans, H. M., Wong, J. Y. & Pföhl, T. (2008). *Biomacromolecules*, **9**, 199–207.
- Köster, S. & Pföhl, T. (2012). *Mod. Phys. Lett. B*, **26**, 1230018.
- Kováčová, G., Grünbein, M. L., Kloos, M., Barends, T. R. M., Schlesinger, R., Heberle, J., Kabsch, W., Shoeman, R. L., Doak, R. B. & Schlichting, I. (2017). *IUCrJ*, **4**, 400–410.
- Makinen, M. W. & Fink, A. L. (1977). *Annu. Rev. Biophys. Bioeng.* **6**, 301–343.
- Mueller, C., Marx, A., Epp, S. W., Zhong, Y., Kuo, A., Balo, A. R., Soman, J., Schotte, F., Lemke, H. T., Owen, R. L., Pai, E. F., Pearson, A. R., Olson, J. S., Anfinrud, P. A., Ernst, O. P. & Dwayne Miller, R. J. (2015). *Struct. Dyn.* **2**, 054302–054317.
- Murshudov, G. N., Skubák, P., Lebedev, A. A., Pannu, N. S., Steiner, R. A., Nicholls, R. A., Winn, M. D., Long, F. & Vagin, A. A. (2011). *Acta Cryst. D* **67**, 355–367.
- Narayanan, T., Wacklin, H., Kononov, O. & Lund, R. (2017). *Crystallogr. Rev.* **23**, 160–226.
- Nogly, P., James, D., Wang, D., White, T. A., Zatsepin, N., Shilova, A., Nelson, G., Liu, H., Johansson, L., Heymann, M., Jaeger, K., Metz, M., Wickstrand, C., Wu, W., Båth, P., Berntsen, P., Oberthuer, D., Panneels, V., Cherezov, V., Chapman, H., Schertler, G., Neutze, R., Spence, J., Moraes, I., Burghammer, M., Standfuss, J. & Weierstall, U. (2015). *IUCrJ*, **2**, 168–176.
- Olmos, J., Pandey, S., Martin-Garcia, J. M., Calvey, G., Katz, A., Knoska, J., Kupitz, C., Hunter, M. S., Liang, M., Oberthuer, D., Yefanov, O., Wiedorn, M., Heymann, M., Holl, M., Pande, K., Barty, A., Miller, M. D., Stern, S., Roy-Chowdhury, S., Coe, J. I., Nagarathnam, N., Zook, J., Verburg, J., Norwood, T., Poudyal, I., Xu, D., Koglin, J., Seaberg, M., Zhao, Y., Bajt, S., Grant, T., Mariani, V., Nelson, G., Subramanian, G., Bae, E., Fromme, R., Fung, R., Schwander, P., Frank, M., White, T., Weierstall, U., Zatsepin, N., Spence, J., Fromme, P., Chapman, H. N., Pollack, L., Tremblay, L., Ourmazd, A., Phillips, G. N. & Schmidt, M. (2018). *BMC Biol.* **16**, 59.
- Owen, R. L., Axford, D., Sherrell, D. A., Kuo, A., Ernst, O. P., Schulz, E. C., Miller, R. J. D. & Mueller-Werkmeister, H. M. (2017). *Acta Cryst. D* **73**, 373–378.
- Pernot, P., Theveneau, P., Giraud, T., Fernandes, R. N., Nurizzo, D., Spruce, D., Surr, J., McSweeney, S., Round, A., Felisaz, F., Foedinger, L., Gobbo, A., Huet, J., Villard, C. & Cipriani, F. (2010). *J. Phys. Conf. Ser.* **247**, 012009.
- Pföhl, T., Otten, A., Köster, S., Dootz, R., Struth, B. & Evans, H. M. (2007). *Biomacromolecules*, **8**, 2167–2172.
- Potterton, L., Agirre, J., Ballard, C., Cowtan, K., Dodson, E., Evans, P. R., Jenkins, H. T., Keegan, R., Krissinel, E., Stevenson, K., Lebedev, A., McNicholas, S. J., Nicholls, R. A., Noble, M., Pannu, N. S., Roth, C., Sheldrick, G., Skubak, P., Turkenburg, J., Uski, V., von Delft, F., Waterman, D., Wilson, K., Winn, M. & Wojdyr, M. (2018). *Acta Cryst. D* **74**, 68–84.
- Roedig, P., Duman, R., Sanchez-Weatherby, J., Vartiainen, I., Burkhardt, A., Warmer, M., David, C., Wagner, A. & Meents, A. (2016). *J. Appl. Cryst.* **49**, 968–975.
- Roessler, C. G., Kuczewski, A., Stearns, R., Ellson, R., Olechno, J., Orville, A. M., Allaire, M., Soares, A. S. & Héroux, A. (2013). *J. Synchrotron Rad.* **20**, 805–808.
- Schmidt, M. (2013). *Adv. Condens. Matter Phys.* **2013**, 1–10.
- Schubert, R., Kapis, S., Gicquel, Y., Bourenkov, G., Schneider, T. R., Heymann, M., Betzel, C. & Perbandt, M. (2016). *IUCrJ*, **3**, 393–401.
- Stagno, J. R., Liu, Y., Bhandari, Y. R., Conrad, C. E., Panja, S., Swain, M., Fan, L., Nelson, G., Li, C., Wendel, D. R., White, T. A., Coe, J. D., Wiedorn, M. O., Knoška, J., Oberthuer, D., Tuckey, R. A., Yu, P., Dyba, M., Tarasov, S. G., Weierstall, U., Grant, T. D., Schwieters, C. D., Zhang, J., Ferré-D'Amaré, A. R., Fromme, P., Draper, D. E., Liang, M., Hunter, M. S., Boutet, S., Tan, K., Zuo, X., Ji, X., Barty, A., Zatsepin, N. A., Chapman, H. N., Spence, J. C. H., Woodson, S. A. & Wang, Y. X. (2017). *Nature*, **541**, 242–246.
- Standfuss, J. & Spence, J. (2017). *IUCrJ*, **4**, 100–101.
- Stellato, F., Oberthür, D., Liang, M., Bean, R., Gati, C., Yefanov, O., Barty, A., Burkhardt, A., Fischer, P., Galli, L., Kirian, R. A., Meyer, J., Panneerselvam, S., Yoon, C. H., Chervinskii, F., Speller, E., White, T. A., Betzel, C., Meents, A. & Chapman, H. N. (2014). *IUCrJ*, **1**, 204–212.
- Sugahara, M., Mizohata, E., Nango, E., Suzuki, M., Tanaka, T., Masuda, T., Tanaka, R., Shimamura, T., Tanaka, Y., Suno, C., Ihara, K., Pan, D., Kakinouchi, K., Sugiyama, S., Murata, M., Inoue, T., Tono, K., Song, C., Park, J., Kameshima, T., Hatsui, T., Joti, Y., Yabashi, M. & Iwata, S. (2015). *Nat. Methods*, **12**, 61–63.
- Sui, S. & Perry, S. L. (2017). *Struct. Dyn.* **4**, 032202.
- Svergun, D. I., Koch, M. H. J., Timmins, P. A. & May, R. P. (2013). *Small Angle X-ray and Neutron Scattering from Solutions of Biological Macromolecules*. Oxford: Oxford University Press.
- Trebbin, M., Steinhäuser, D., Perlich, J., Buffet, A., Roth, S. V., Zimmermann, W., Thiele, J. & Förster, S. (2013). *Proc. Natl Acad. Sci.* **110**, 6706–6711.
- Uzawa, T., Akiyama, S., Kimura, T., Takahashi, S., Ishimori, K., Morishima, I. & Fujisawa, T. (2004). *Proc. Natl Acad. Sci.* **101**, 1171–1176.
- Vagin, A. & Teplyakov, A. (1997). *J. Appl. Cryst.* **30**, 1022–1025.
- Wang, C. W., Sinton, D. & Moffitt, M. G. (2011). *J. Am. Chem. Soc.* **133**, 18853–18864.
- Warkentin, M., Hopkins, J. B., Badeau, R., Mulichak, A. M., Keefe, L. J. & Thorne, R. E. (2013). *J. Synchrotron Rad.* **20**, 7–13.
- Weinert, T., Olieric, N., Cheng, R., Brünle, S., James, D., Ozerov, D., Gashi, D., Vera, L., Marsh, M., Jaeger, K., Dworkowski, F., Panepucci, E., Basu, S., Skopintsev, P., Doré, A. S., Geng, T., Cooke, R. M., Liang, M., Protá, A. E., Panneels, V., Nogly, P., Ermler, U., Schertler, G., Hennig, M., Steinmetz, M. O., Wang, M. & Standfuss, J. (2017). *Nat. Commun.* **8**, 542.
- White, T. A. (2014). *Philos. Trans. R. Soc. B: Biol. Sci.* **369**, 20130330.
- White, T. A., Mariani, V., Brehm, W., Yefanov, O., Barty, A., Beyerlein, K. R., Chervinskii, F., Galli, L., Gati, C., Nakane, T., Tolstikova, A., Yamashita, K., Yoon, C. H., Diederichs, K. & Chapman, H. N. (2016). *J. Appl. Cryst.* **49**, 680–689.
- With, S., Trebbin, M., Bartz, C. B. A., Neuber, C., Dulle, M., Yu, S., Roth, S. V., Schmidt, H.-W. & Förster, S. (2014). *Langmuir*, **30**, 12494–12502.
- Yamamoto, M., Hirata, K., Yamashita, K., Hasegawa, K., Ueno, G., Ago, H. & Kumasaka, T. (2017). *IUCrJ*, **4**, 529–539.
- Zarrine-Afsar, A., Barends, T. R. M., Mueller, C., Fuchs, M. R., Lomb, L., Schlichting, I. & Miller, R. J. D. (2012). *Acta Cryst. D* **68**, 321–323.
- Zeldin, O. B., Brockhauser, S., Bremridge, J., Holton, J. M. & Garman, E. F. (2013). *Proc. Natl Acad. Sci.* **110**, 20551–20556.
- Zeldin, O. B., Gerstel, M. & Garman, E. F. (2013). *J. Appl. Cryst.* **46**, 1225–1230.